Physics of the Solid State, 2026, Vol. 68, No. 2

01,07

Plastic deformation effect on formation of nanocrystals in Co-based amorphous alloys

© G.E. Abrosimova, D.I. Jimenez Remache, V.V. Chirkova, A.S. Aronin

Institute of Solid State Physics, RAS,
Chernogolovka, Russia

E-mail: gea@issp.ac.ru

Received November 25, 2025
Revised November 25, 2025
Accepted January 30, 2026

The impact of deformation on crystallization of $Co_{67}Si_{12}B_9Fe_7Nb_5$ amorphous alloy has been studied by methods of X-ray, scanning and transmission electron microscopy. It was found that deformation leads to the formation of a heterogeneous amorphous structure consisting of shear bands (areas of reduced density) and a non-deformed amorphous matrix surrounding them. The average change in the distance between the atoms in a deformed amorphous alloy compared to the non-deformed one is 0.12 %. Because of the formed reduced density regions the crystallization processes is accelerated and a material with a higher proportion of the crystalline phase may be obtained. The formation of nanocrystals with a body-centered cubic (BCC) lattice in an amorphous cobalt alloy is discussed under the assumption that a crystal nucleation occurs in the ordered regions where the short-range order corresponds to that of the BCC-phase being formed.

Keywords: amorphous phase, shear bands, nanocrystallization, transmission electron microscopy, X-ray analysis.

DOI: 10.61011/PSS.2026.02.63374.8823

1. Introduction

Developing the methods for fabrication of a composite amorphous nanocrystalline structure opens up new ways to create useful materials. Formation of nanocrystals in the amorphous phase of many alloys provides a way better physical and chemical properties of these alloys [1–6]. When nanocrystals are formed in amorphous alloys of iron and cobalt their magnetic properties noticeably improve, and in aluminum and zirconium alloys this results in higher strength with good ductility, etc. Such a change can be very significant. Thus, in the amorphous alloy $Fe_{75}Si_{11}B_{10}Nb_3Sn_1$ the coercive force makes 5 A/m and when annealed to a temperature of 500 °C it declines, however, with further temperature rise to 530 °C the coercive force increases by three orders of magnitude reaching as high as 4.4 kA/m. Heat treatments at higher temperatures lead to a further increase in coercive force, although at a slower rate [3]. Thus, structural relaxation helps to soften the magnetic characteristics of amorphous alloys, magnetic hardening is observed during crystallization: partially crystalline alloys are soft-magnetic, and fully crystallized alloys are hard-magnetic. Alloy $Fe_{73.8}Cu_1Nb_{3.1}B_{9.1}Si_{13}$ in its amorphous state has a positive saturation magnetostriction (about $30 \cdot 10^{-6}$) [1]; during crystallization, nanocrystals of a solid Si solution are formed in Fe, which has negative magnetostriction helping to compensate for the positive magnetostriction of the amorphous matrix. Eventually, this leads to formation of a material with an almost zero magnetostriction. When an amorphous nanocrystalline structure is generated in $Fe_{73.8}Cu_1Nb_{3.1}B_{9.1}Si_{13}$ alloy a huge growth of permeability (up to hundreds of thousands units) is observed.

An example of a fundamental change in mechanical properties is demonstrated by the study of a bulk amorphous alloy $Zr_{50}Ti_{16.5}Cu_{14}Ni_{18.5}$ during heating *in situ*. In tensile tests under heating *in situ* [7], the flow stress and fracture stress decrease monotonously with increasing temperature, and the rate of decrease in flow stress is higher than the rate of decrease in fracture stress. At temperatures below 325 K, a brittle-ductile transition occurs. At 775 K the plastic strain reaches its record value of 335 %.

Heat treatment or deformation is usually used to form an amorphous nanocrystalline composite structure [8–13]. Composite amorphous-nanocrystalline structures formed during heat treatment and deformation turn out to be different, and the observed differences depend both on the conditions of external influences and on the chemical composition of the alloy.

The difference in the phase composition of amorphous nanocrystalline alloys which crystallize during heat treatment and deformation is clearly evident in zirconium alloys. When heat-treating the amorphous alloy $Zr_{55}Cu_{30}Al_{15}Ni_5$ the crystallization initiates from the formation of a metastable phase with a hexagonal structure of space group $P6_3/mmc$ with parameters $a = 8.66$ Å, $c = 14.99$ Å, and in case of strain an equilibrium crystalline phase of Zr_2Cu emerges with a lattice of spatial group $Fd3m$ [13]. Studies of the crystallization of amorphous alloy $Zr_{50}Ti_{16.5}Cu_{14}Ni_{18.5}$ during stretching at elevated temperatures have shown that the portion of crystalline phase rises when a higher strain is applied [7].

A significant difference is also observed in the localization of nanocrystals formed by heating and deformation of [8,11–15]: in the amorphous phase after heat treatment, the nanocrystals are chaotically distributed more or less uniformly over the specimen, and in case of a deformed material they are located in the area of deformation localization (in shear bands and their neighborhood) [16–20]. In the study of a group of light aluminum-based alloys, it was found that nanocrystals of smaller sizes are formed during plastic deformation than during heat treatment [21]. For a number of amorphous alloys, the dependence of the forming nanostructure on the initial state of the amorphous phase before the start of crystallization was also established: whether the amorphous structure was homogeneous or heterogeneous.

How typical are such differences and are they typical for amorphous alloys of different chemical compositions? This article is focused on the study of the deformation effect on crystallization of an amorphous cobalt-based alloy. The interest in these alloys may be caused due to two reasons. Firstly, cobalt-based amorphous alloys are ferromagnetic and have high magnetic properties. They have a lower saturation magnetization compared to iron-based alloys, but a higher Curie temperature [22], which is an evidence of their potential usage at higher temperatures. The second value is associated with a specific process of the alloys crystallization. As seen in the phase equilibrium diagrams during the primary crystallization of cobalt-based amorphous alloys, it is natural to expect the formation of crystals with a hexagonal close-packed (HCP) lattice or a metastable phase with a face-centered cubic (FCC) lattice (cobalt lattices), however, in cobalt alloys doped with a small amount components with a body-centered cubic (BCC) lattice [23], the formation of a BCC phase was detected. The studies outlined in [23], covered the crystallization of amorphous phase during heat treatment. Due to the described difference in the amorphous-crystalline structure formed during heat treatment and deformation, it was interesting to investigate the deformation effect on crystallization of an amorphous cobalt alloy doped with components having a BCC-lattice.

2. Experimental procedure

The initial alloy $Co_{67}Si_{12}B_9Fe_7Nb_5$ was fabricated by arc melting in purified argon of pure ($> 99.9\,\%$) components. Amorphous alloy as a ribbon $30\,\mu$m long and ~ 1 cm wide was obtained by method of a rapid melt quenching, with the melt cooling rate of 10^6 K/s. The composition of the quenched ribbons was controlled by local X-ray microanalysis using Zeiss Supra 50VP scanning electron microscope appliance. Except for Boron, all components were detected with an accuracy of 0.1 %. The specimens were subjected to heat treatment followed by application of deformation. Heat treatment (isothermal annealing for 1 h at different temperatures) was carried out in a SUOL resistance furnace, deformation was applied by repeated rolling at room temperature on a laboratory rolling mill VEB Schwermaschinenbau. The strain degree was found by the formula

$$\varepsilon = (h_0 - h_1)/h_0,$$

where h_0 and h_1 — thickness of the specimen before and after deformation, accordingly.

The specimens surface was studied using ZeissSupra 50VP scanning electron microscope (SEM). X-ray diffraction studies were performed on Siemens D-500 X-ray diffractometer using Co$K_\alpha$radiation. The specimens microstructure was studied by transmission electron microscopy (TEM) on a JEOL-100 CXII electron microscope; the foils for electron microscopic studies were prepared by ion thinning. The structure was monitored at each stage of the specimen treatment (after quenching, annealing, and/or deformation), and special substrates that had no own reflections were used during X-ray diffraction studies [24]. When processing the spectra, programs were used that enabled to carry out smoothing, background correction, and separation of overlapping maxima. The size of nanocrystals was estimated by FWHM of the diffraction maximum [25].

3. Experimental results

After fabrication the ribbons were amorphous. Figure 1 shows an X-ray diffraction pattern of the initial alloy, which contains only diffuse reflections characteristic of the amorphous phase. Figure 2 shows an electron microscopic image of the amorphous alloy immediately after its fabrication.

As noted above, the specimens were deformed by repeated rolling at room temperature. The image of the surface of the deformed alloy obtained by scanning electron microscopy is shown in Figure 3. The figure shows the irregularities of the relief — the places where the shear bands exit onto the specimen surface.

The change in the structure in deformation of an amorphous alloy depends on the strain degree. With a small

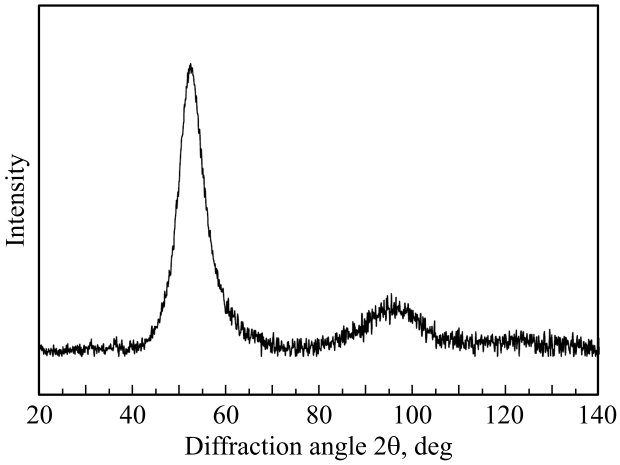

Figure 1. X-ray diffraction pattern of the initial amorphous alloy.

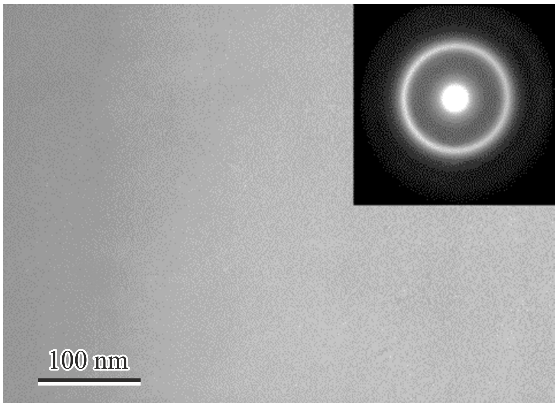

Figure 2. TEM-image of the initial amorphous alloy.

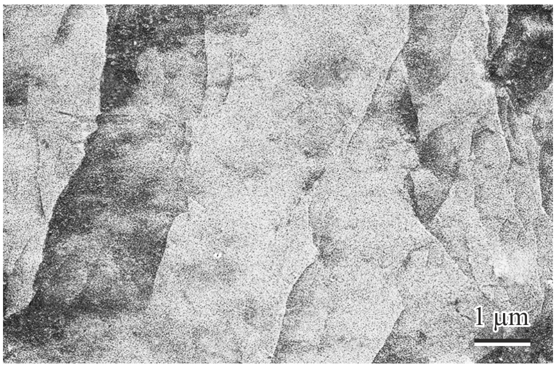

Figure 3. SEM-image of the deformed alloy surface.

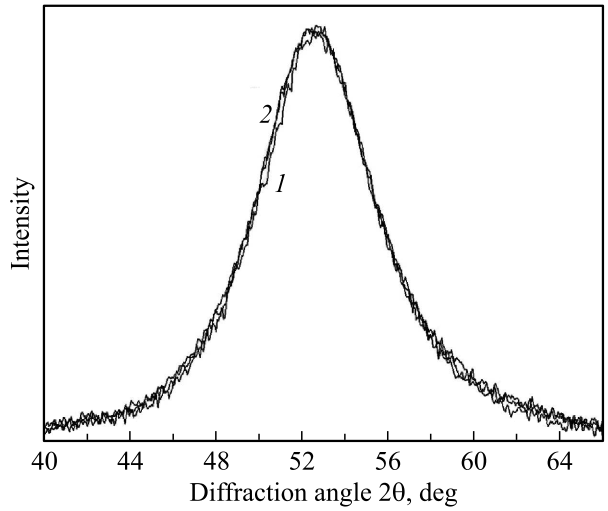

Figure 4. X-ray diffraction patterns of specimens with a 2 % (curve *1*) and 8 % (*2*) strain degree.

strain degree (2 %), the position of the diffuse maximum on the X-ray diffraction pattern practically does not differ from its position on the X-ray diffraction patterns of the original non-deformed specimen (the displacement of the diffuse maximum to the region of smaller angles is on the verge of measurement accuracy), with the rise of strain degree, this difference increases. Figure 4 shows the X-ray diffraction patterns of specimens deformed by 2 % (curve *1*) and 8 % (curve *2*) — only the region of the first diffusion maximum is given for clarity.

It should be noted that, despite the seemingly identical X-ray diffraction patterns, the average radius of the first coordination sphere (the shortest distance between atoms) differs.

As is known, the intensity of X-ray scattering by the amorphous phase is determined by the formula

$$I(\mathbf{S}) = NF^2(\mathbf{S})\left\{1+\int_0^\infty 4\pi R^2[\rho(R)-\rho_0]\sin(SR)/(SR)dR\right\},$$

where N — total number of atoms per unit volume, $F(S)$ — scattering amplitude, $\rho(R)$ — number of atoms per unit volume located at a distance of R from the selected atom, ρ_0 — average number of atoms per unit volume, S — parameter related to the wave vector [26]. The sequence of maxima of $I(S)$ is determined by the sequence of maxima of $\sin(SR)/(SR)$ function. This function has its maxima at the values SR equal 7.73, 14.06, 20.46 and etc., while the first coordination sphere radius R_1 makes

$$R_1 = 7.73/S_1 = 14.06/S_2 = 20.46/S_3 \ldots$$

It is clear that the radius of the first coordination sphere can be determined from the wave vector magnitude corresponding to any maximum of the scattering intensity curve. Usually, the position of the first maximum is used for this, since it is the most intense one [27]. According to Ehrenfest equation, the value of R_1 is [26]

$$2R_1 \sin\theta = 1.23\lambda,$$

where λ — the wavelength of the radiation used, θ — diffraction angle.

The radius of the first coordination sphere of the initial specimen determined in this way is $R_{1,0} = 2.479$ Å, and that of the deformed one — $R_{1,\text{deform}} = 2.482$ Å. This means that the change in the distance between atoms under the applied deformation conditions is $\Delta R_1 = R_{1,\text{deform}} - R_{1,0} = 0.003$ Å, i.e. 0.12 %.

Using these values, we can estimate the change in free volume ΔV as a result of deformation using the formula [27]

$$\Delta V = (R^3_{1,\text{deform}} - R^3_{1,0})/R^3_{1,0} \cdot 100\,\%.$$

This is consistent with the increase of free volume ΔV by 0.36 %.

The initial and deformed specimens were annealed simultaneously.

Figure 5 illustrates the X-ray images of alloys annealed at 460 °C for 1 h. It can be seen that during the preliminary deformation, the intensity of the maximum increases, and its FWHM declines. Lower FWHM of the diffuse maximum on the X-ray diffraction pattern indicates that there's a

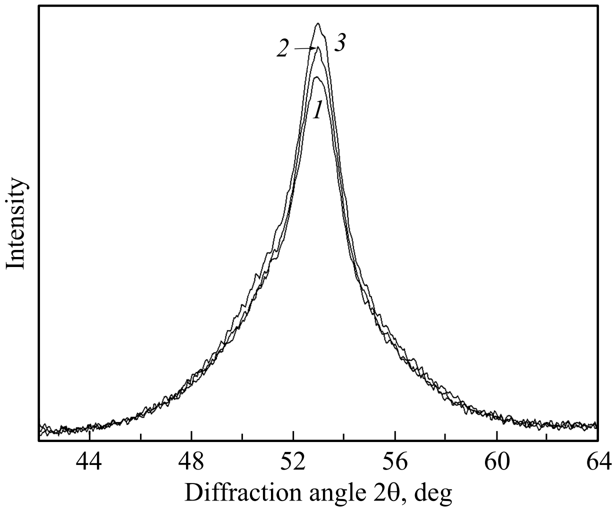

Figure 5. X-ray diffraction patterns of initial specimen (curve *1*) and specimens deformed by 2% (*2*) and 8% (*3*) after an hour annealing at 460 °C.

Table 1. The proportion of nanocrystalline phase in the annealed specimens depends on the degree of pre-deformation

Degree strain, %	Proportion of the nanocrystalline phase, %
0	13
2	17
8	21

diffraction contribution to the curve, i.e., crystals appear in the amorphous phase. To estimate the proportion of nanocrystals, the observed maxima were separated into a diffuse component from the amorphous phase and into a diffraction component from the nanocrystals. The standard program [20,27,28] was used for expansion using Voigt function, which is a combination of Gauss and Lorentz functions. Figure 6 shows the expansions of X-ray diffraction patterns of the annealed specimens without pre-deformation (Figure 6, *a*) and after pre-deformation by 2% (Figure 6, *b*) and 8% (Figure 6, *c*). Curve *1* — experimental, *2* — amorphous phase scattering curve, *3* — diffraction reflection from nanocrystals, *4* — sum of curves *2* and *3*.

The average crystal sizes were determined from FWHM of the diffraction peaks and Selyakov-Scherrer formula [25]. The size of nanocrystals in an annealed specimen without preliminary deformation is 6 nm, and in specimens deformed by 2 and 8% — 5.9 and 6 nm, respectively. Within the limits of experimental accuracy, the average size of nanocrystals is the same. Unlike the size, the proportion of nanocrystals depends on the treatment conditions. Table 1 shows proportions of the nanocrystalline phase depending on the strain degree.

It can be seen that as the strain degree rises, the proportion of the nanocrystalline phase increases.

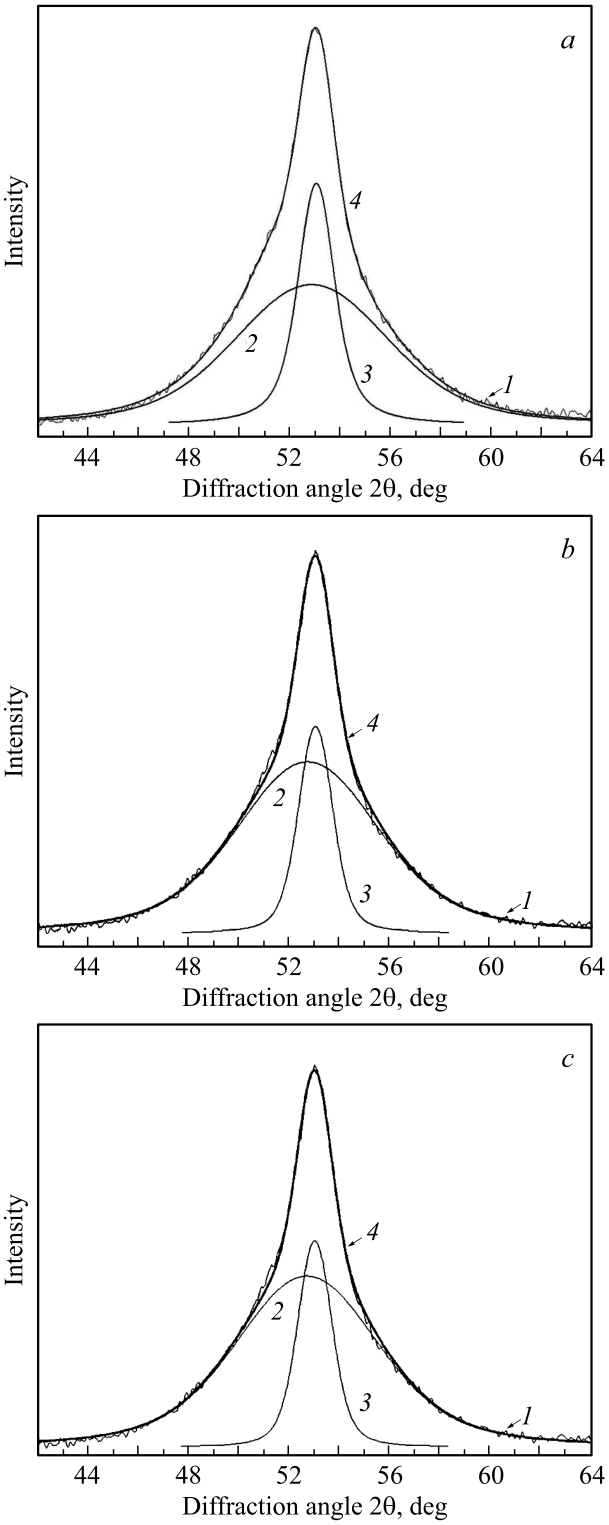

Figure 6. *a* — X-ray diffraction pattern of the initial specimen after annealing for 1 hour at 460 °C; *b* — X-ray diffraction pattern of specimen deformed by 2%, after annealing for 1 hour at 460 °C; *c* — X-ray of specimen deformed by 8%, after annealing for 1 hour at 460 °C.

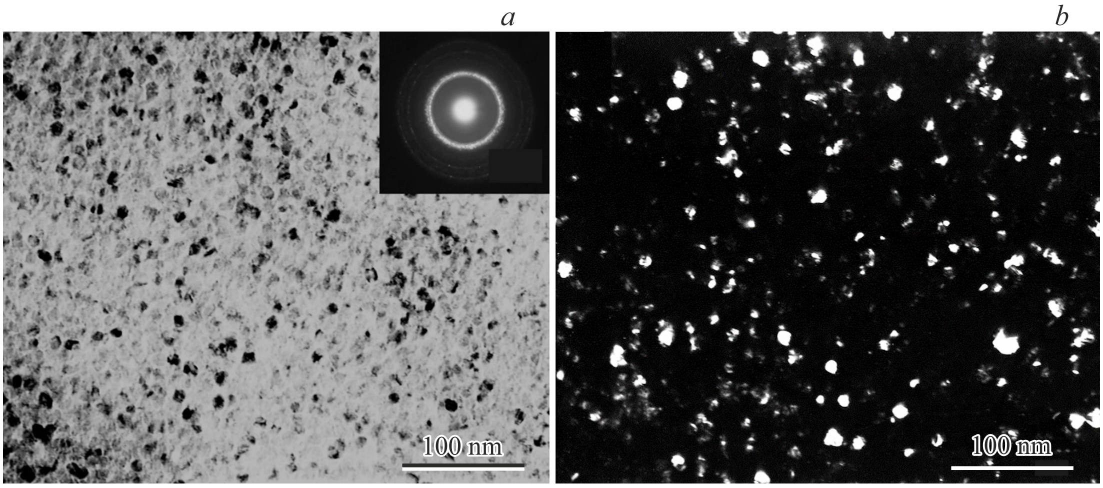

Figure 7. Bright-field (*a*) and dark-field (*b*) electron microscopic images of annealed specimens without pre-deformation.

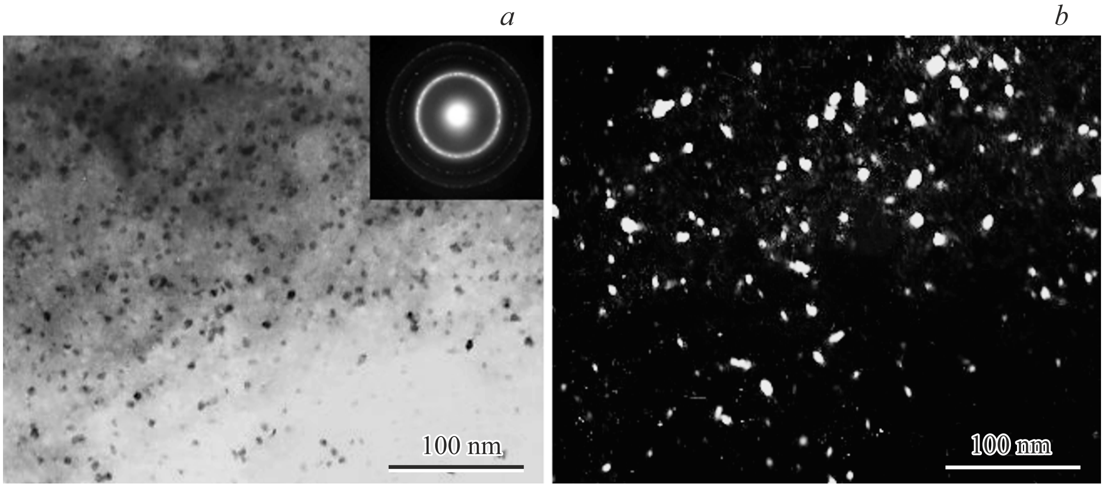

Figure 8. Bright-field (*a*) and dark-field (*b*) electron microscopic images of annealed specimens with pre-deformation of 2 %.

Figures 7 and 8 show bright-field and dark-field electron microscopic images of annealed specimens without pre-deformation (Figure 7) and with a preliminary deformation of 2 % (Figure 8). The insets to the bright-field images show the corresponding electron diffraction patterns, which show both a diffuse halo from the amorphous phase and point reflections from the nanocrystals.

Using dark-field images, the average size of nanocrystals was determined across 500 measurements, and this size was 6.2 and 6.1 nm for the non-deformed and deformed specimen, respectively. These values practically coincide with the results obtained by X-ray diffraction method. Comparative values of the average sizes of nanocrystals obtained by different methods are given in Table 2.

As the annealing temperature rises, the proportion of the crystalline phase increases. After annealing at 600 °C the specimens contain FCC-Co [29], BCC-phase and $Co_{16}Nb_6Si_7$ (lattice of space group $Fm\bar{3}m$ (225), $a = 11.235$ Å) [30], as well as remaining amorphous phase (a diffuse halo in the region $\sim 48-58°$). Figure 9 demonstrates the X-ray diffraction patterns of specimens annealed at 600 °C for 1 h: without pre-deformation (curve *1*) and after deformation 2 % (*2*) and 8 % (*3*). BCC- and FCC-phases actually represent themselves the solid solutions of the alloy components.

The phase composition of the annealed specimens is the same, but the proportion of the crystalline phase in them is different. The inset to Figure 9 shows the area of the most intense reflections. It can be seen that with the higher strain degree the proportion of phase $Co_{16}Nb_6Si_7$ rises. Higher intensity of diffraction reflections also indicates a decrease in the proportion of amorphous phase in the specimen. The largest proportion of the crystalline component of the structure is observed after deformation of 8 %, the smallest — in the non-deformed specimen. As shown above, the same trend was observed after annealing at a

Table 2. The average crystal size determined by transmission electron microscopy and X-ray diffraction analysis

Specimen	Average crystal size d, nm	
	Transmission electron microscopy	X-ray diffraction analysis
Annealing without pre-rolling	6.2	6
Annealed after deformation 2 %	6.1	5.9
Annealed after deformation 8 %	–	6

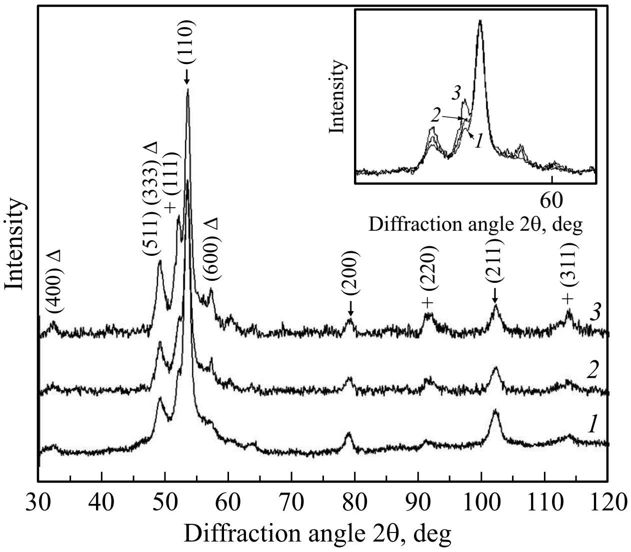

Figure 9. X-ray diffraction patterns of specimens annealed at 600 °C for 1 h: without pre-deformation (curve *1*) and after deformation 2 % (*2*) and 8 % (*3*). Reflections from phase $Co_{16}Nb_6Si_7$ are designated by triangles, from BCC-phase — by arrows, from FCC-phase — by criss-cross.

lower temperature (at 460 °C). Thus, pre-deformation helps to accelerate the crystallization processes.

4. Discussion of findings

The results obtained can be roughly divided into three groups.

1) Even with a slight deformation of the amorphous alloy, a shift of the diffuse maximum in the X-ray diffraction patterns to a region of smaller angles is observed. As noted above, the change in the radius of the first coordination sphere (the distance between atoms) is about 0.12 %. Such a change indicates the appearance of regions of lower density in the specimen — shear bands. It is known that plastic deformation in amorphous alloys is highly localized and leads to the formation of shear bands [8,31–37]. The thickness of the shear bands is 5–20 nm [32,35,37], their structure is complex, and changes in the structure of the amorphous phase can propagate over long distances from the shear band, up to 200 nm. The amorphous phase in the shear bands has a lower density compared to the surrounding amorphous matrix [32], and the density difference may reach 10 % [32,36]. In these areas, the processes of diffusion mass transfer are noticeably facilitated. It was found that the diffusion coefficient in the shear bands at room temperature is 5–6 times higher than in the surrounding amorphous matrix [38], which may result in accelerated crystallization. The degree of structural change in the shear band naturally depends on the deformation conditions. The nanocrystals are initiated in the shear bands and their neighborhood [8]. During deformation, nanocrystals are formed even in alloys where they are not formed during heat treatment. As a result of deformation, the structure of the amorphous alloy becomes heterogeneous and is itself a kind of nanoglass; the amorphous phase consists of regions of different densities: regions of shear bands (with lower density) and non-deformed amorphous phase (with higher density).

Consequently, as a result of deformation, the amorphous structure becomes heterogeneous and consists of shear bands (areas of reduced density) and surrounding areas of non-deformed amorphous matrix. This means that the observed changes in the radius of the first coordination sphere represent the „average“ value for the specimen. R_1 is an averaged value [27]

$$R_1 = (a \cdot R_{1,\text{specimen}} + b \cdot R_{1,\text{shear band}}),$$

where a and b — the volume fractions of the unchanged amorphous phase and the shear bands, respectively. Since the volume fraction of the shear bands is small, the change in the average radius of the first coordination sphere

$$\Delta R_1 = R_{1,\text{deform}} - R_{1,0}$$

shall be small which is observed experimentally.

Thus, the deformation of amorphous alloy leads to the formation of a heterogeneous amorphous structure consisting of regions of different densities and, as a result, with different parameters of diffusion mass transfer.

2) As noted above, shear bands are places of reduced density or, in other words, areas with a high content of free volume. The free volume plays an important role in the crystallization of the amorphous phase. The quenched alloys inherit the density of the melt, with structural

relaxation the free volume declines and it rises with deformation [39,40]. There are many studies highlighting the changes in free volume during deformation of amorphous alloys [32–34,38,40–45]. With the observed, seemingly small amount of change in the distance between atoms and a small change in the free volume δV ($\sim 0.36\,\%$), these changes are enough to accelerate the crystallization processes. It should be stressed that the impact of the amorphous phase structure (homogeneous or heterogeneous) persists even with the growth of the annealing temperature. Figure 5 shows the difference in the structure of the annealed specimens at 460 °C after various strain degree (curves *2* and *3*). It can be seen that as the strain degree increases, the proportion of the crystalline phase becomes larger. After annealing at a higher temperature (600 °C, Figure 9), the difference persists: with the same phase composition, the proportion of the crystalline component of the structure rises. This is especially visible on the reflections of $Co_{16}Nb_6Si_7$ phase (Figure 9, inset). With an increase in the strain degree (an increase in the number of areas of reduced density and, consequently, areas of accelerated mass transfer), the amount of the crystalline phase increases. It is also important to note that the size of nanocrystals does not depend on the strain degree.

Heterogeneous amorphous structure in amorphous alloys can be formed both as a result of chemical redistribution of components (formation of regions enriched with one or another component of the alloy during low-temperature annealing, which does not lead to crystallization), and as a result of deformation (formation of regions of different densities). Earlier, when studying amorphous aluminum-based alloys, it was found that the proportion of nanocrystals formed in a heterogeneous amorphous structure during subsequent annealing is higher in preformed specimens than in the pre-annealed ones [21]. The same pattern is observed in cobalt alloys (Figs. 5 and 9, curve *1* in both figures).

Thus, the formation of areas of reduced density as a result of the deformation of the amorphous phase accelerates the crystallization processes and makes it possible to obtain a material with a higher proportion of the crystalline phase.

3) It is known that the crystallization of amorphous alloys of the metal-metalloid group of pre-eutectic composition usually starts with formation of crystals of the alloy's main component or a solid solution based on it. As mentioned above, it has been recently discovered that in Co-Si-B-M alloys (where $\mathrm{M} = \mathrm{Fe, Nb}$) the crystallization starts with release of BCC-phase instead of the expected crystals with FCC- or HCP-lattice corresponding to the crystalline modifications of cobalt. The formation of a BCC phase was observed in an amorphous cobalt-based alloy doped with components with a BCC lattice [23]. Earlier the formation of BCC-phase, typical for Fe phase, was observed in Co alloys only at quite high iron concentration (with the ratio Co:Fe at least 2 : 1, e. g., 65 % Co and 35 % Fe [46,47]), however, in the latest studies Fe concentration was 5−10 at. % and was no higher than 16 at. %. The conducted studies [23,48,49] allowed to find the dependence of BCC phase formation on the concentration of alloying components with a BCC-lattice and showed that nanostructure parameters (size and proportion of nanocrystals) depend on their concentration. Papers [23,48,49] describe the studies made during the amorphous alloys heat treatment. In this paper, the crystallization of amorphous alloys subjected to plastic deformation was investigated. It was found that the alloys annealed after deformation and without pre-deformation had the same phase composition; only the fraction of crystalline phase differed. The reasons for the formation of a structure atypical for cobalt-based alloys during heat treatment were discussed in detail in [23,48,49]. It has been shown that crystal nucleation and growth occur in the ordered regions enriched in doping components that have a BCC lattice (Fe, Nb), where the short-range order corresponds to the short-range order of the BCC phase.

5. Conclusion

Studies of the cold rolling deformation effect on crystallization in the amorphous alloy $Co_{67}Si_{12}B_9Fe_7Nb_5$ have shown that

- deformation of an amorphous alloy leads to the formation of a heterogeneous amorphous structure consisting of shear bands (regions of reduced density) and surrounding regions of an non-deformed amorphous matrix; the average change in the distance between atoms in a deformed amorphous alloy compared with the non-deformed alloy is 0.12 %;
- in the deformation conditions used, the change in the free volume ΔV makes 0.36 %; the formation of reduced density regions as a result of deformation accelerates the crystallization processes and makes it possible to obtain a material with a greater proportion of the crystalline phase;
- the effect of the amorphous phase state (homogeneous or heterogeneous structure) before the start of crystallization persists even during annealing at elevated temperatures (up to 600 °C);
- the formation of nanocrystals with a BCC lattice in an amorphous cobalt alloy is discussed under the assumption that a crystal nucleation occurs in the ordered regions where the short-range order corresponds to that of the BCC-phase being formed.

Funding

The study was performed under the State Assignment of ISSP of RAS.

Conflict of interest

The authors declare no conflict of interest.

References

[1] G. Herzer. Physica Scripta **1993**, *T49A*, 307 (1993). https://doi.org/10.1088/0031-8949%2F1993%2FT49A%2F054

[2] G. Herzer. J. Magn. Magn. Mater. **294**, *2*, 99 (2005). https://doi.org/10.1016/j.jmmm.2005.03.020

[3] V. Cremanshi, B. Arcondo, H. Sirkin, M. Vazquez, F. Asenjo, J.M. Garcia, G. Abrosimova, A. Aronin. J. Mater. Res. **15**, *9*, 1936 (2000).

[4] H. Chiriac, T.A. Óvári. Progr. Mater Sci. **40**, *5*, 333 (1996). https://doi.org/10.1016/S0079-6425(97)00001-7

[5] Zs. Kovács, P. Henits, S. Hóbor, Ó. Róvósz. Rev. Adv. Mater. Sci. **18**, *7*, 593 (2008).

[6] N.N. Sitnikov, A.V. Shelyakov, R.V. Sundeev, I.A. Khabibullina. FTT **62**, *5*, 649 (2020) (in Russian). https://doi.org/10.21883/FTT.2020.05.49223.14M [N.N. Sitnikov, A.V. Shelyakov, R.V. Sundeev, I.A. Khabibullina. Phys. Solid State **62**, *5*, 733 (2020).]

[7] G.E. Abrosimova, A.S. Aronin, D.V. Matveev, I.I. Zver'kova, V.V. Molokanov, S. Pan, A. Slipenyuk. J. Mater. Sci. **36**, *16*, 3933 (2001).

[8] A.L. Greer, Y.Q. Cheng, E. Ma. Mater. Sci. Eng.: R: Rep. **74**, *4*, 71 (2013). https://doi.org/10.1016/j.mser.2013.04.001

[9] N. Boucharat, R. Hebert, H. Rösner, R.Z. Valiev, G. Wilde. J. Alloys. Compd. **434**–**435**, 252 (2007). https://doi.org/10.1016/j.jallcom.2006.08.128

[10] J. Eckert, M. Calin, P. Yu, L.C. Zhang, S. Scudino, C. Duhamel. Rev. Adv. Mater. Sci. **18**, *2*, 169 (2008). https://www.ipme.ru/e-journals/RAMS/no_21808/eckert.pdf

[11] G. Wilde, H. Rösner. Appl. Phys. Lett. **98**, *25*, 251904 (2011). https://doi.org/10.1063/1.3602315

[12] G.Z. Ma, K.K. Song, B.A. Sun, Z.J. Yan, U. Kühn, D. Chen, J. Eckert. J. Mater. Sci. **48**, *19*, 6825 (2013). https://doi.org/10.1007/s10853-013-7488-1

[13] N. Boucharat, R. Hebert, H. Rösner, R. Valiev, G. Wilde. Scripta Materialia **53**, *7*, 823 (2005). https://doi.org/10.1016/j.scriptamat.2005.06.004

[14] J. Pan, Q. Chen, L. Liu, Y. Li. Acta Materialia **59**, *13*, 5146 (2011). https://doi.org/10.1016/j.actamat.2011.04.047

[15] R.J. Hebert, N. Boucharat, J.H. Perepezko, H. Rösner, G. Wilde. J. Alloys Compd. **434**–**435**, 18 (2007). https://doi.org/10.1016/j.jallcom.2006.08.134

[16] R. Maaß, J.F. Löffler. Adv. Funct. Mater. **25**, *16*, 2353 (2015). https://doi.org/10.1002/adfm.201404223

[17] S.J. Kang, Q.P. Cao, J. Liu, Y. Tang, X.D. Wang, D.X. Zhang, I.S. Ahn, A. Caron, J.Z. Jiang. J. Alloys. Compd. **795**, 493 (2019). https://doi.org/10.1016/j.jallcom.2019.05.026

[18] D. Şopu, S. Scudino, X.L. Bian, C. Gammer, J. Eckert. Scripta Materialia **178**, 57 (2020). https://doi.org/10.1016/j.scriptamat.2019.11.006

[19] A. Hassanpour, M. Vaidya, S.V. Divinski, G. Wilde. Acta Materialia **209**, 116785 (2021). https://doi.org/10.1016/j.actamat.2021.116785

[20] G. Abrosimova, B. Gnesin, D. Gunderov, A. Drozdenko, D. Matveev, B. Mironchuk, E. Pershina, I. Sholin, A. Aronin. Metals **10**, *10*, 1329 (2020). https://doi.org/10.3390/met10101329

[21] A. Aronin, A. Budchenko, D. Matveev, E. Pershina, G. Tkatch, G. Abrosimova. Rev. Adv. Mater. Sci. **46**, *1*, 53 (2016).

[22] D. Huang, Y. Li, Y. Yang, Z. Zhu, W. Zhang. J. Alloys. Compd. **843**, 154862 (2020). https://doi.org/10.1016/j.jallcom.2020.154862

[23] G.E. Abrosimova, N.A. Volkov, E.A. Pershina, V.V. Chirkova, I.A. Sholin, A.S. Aronin. J. Non Cryst. Solids **565**, 120864 (2021). https://doi.org/10.1016/j.jnoncrysol.2021.120864

[24] G.E. Abrosimova, I.M. Shmytko. Zavodskaya laboratoriya. Diagnostika materialov, **84** *6*, 34 (2018) (in Russian). https://doi.org/10.26896/1028-6861-2018-84-6-34-37

[25] A. Guinier. Théorie et Technique de La Radiocristallographie. Dunod, Paris (1956).

[26] A.F. Skryshevsky. Strukturnyj analiz zhidkostej i amorfnykh tel. Vysshaya shkola, M. (1980). 328 p. (in Russian).

[27] G.E. Abrosimova, V.V. Astanin, N.A. Volkov, D.V. Gunderov, E.Yu. Postnova, A.S. Aronin. FMM **124**, *7*, 622 (2023) (in Russian). https://doi.org/10.31857/S001532302 3600521

[28] G. Abrosimova, N. Volkov, T.V. Tuan, E. Pershina, A. Aronin. Mater. Lett. **240**, 150 (2019). https://doi.org/10.1016/j.matlet.2018.12.131

[29] PAULING FILE / Ed. P. Villars. In: Inorganic Solid Phases, Springer Materials (online database). Springer-Verlag GmbH, Heidelberg (2024). https://materials.springer.com/isp/crystallographic/docs/sd_0261115sd_0261115

[30] PAULING FILE / Ed. P. Villars. In: Inorganic Solid Phases, Springer Materials (online database). (Springer-Verlag GmbH, Heidelberg (2024). https://materials.springer.com/isp/crystallographic/docs/sd_1006167sd_1006167

[31] W.H. Jiang, M. Atzmon. Acta Materialia **51**, *14*, 4095 (2003). https://doi.org/10.1016/S1359-6454(03)00229-5

[32] H. Rösner, M. Peterlechner, C. Kübel, V. Schmidt, G. Wilde. Ultramicroscopy **142**, 1 (2014). https://doi.org/10.1016/j.ultramic.2014.03.006

[33] R. Maaß, P. Birckigt, C. Borchers, K. Samwer, C.A. Volkert. Acta Materialia **98**, 94 (2015). https://doi.org/10.1016/j.actamat.2015.06.062

[34] V. Schmidt, H. Rösner, M. Peterlechler, G. Wilde, P.M. Voyles. Phys. Rev. Lett. **115**, *3*, 035501 (2015). https://doi.org/10.1103/PhysRevLett.115.035501

[35] J. He, I. Kaban, N. Mattern, K. Song, B. Sun, J. Zhao, D.H. Kim, J. Eckert, A.L. Greer. Sci. Rep. **6**, *1*, 25832 (2016). https://doi.org/10.1038/srep25832

[36] C. Liu, V. Roddatis, P. Kenesei, R. Maaß. Acta Materialia **140**, 206 (2017). https://doi.org/10.1016/j.actamat.2017.08.032

[37] J. Li, Z.L. Wang, T.C. Hufnagel. Phys. Rev. B **65**, *14*, 144201 (2002). https://doi.org/10.1103/PhysRevB.65.144201

[38] A.S. Aronin, D.V. Louzguine-Luzgin. Mech. Mater. **113**, 19 (2017). https://doi.org/10.1016/j.mechmat.2017.07.007

[39] A.R. Yavari, A.L. Moulec, A. Inoue, N. Nishiyama, N. Lupu, E. Matsubara, W.J. Botta, G. Vaughan, M.D. Michiel, Å. Kvick. Acta Materialia **53**, 1611 (2005).

[40] S. Chen, D. Xu, X. Zhang, X. Chen, Y. Liu, T. Liang, Z. Yin, S. Jiang, K. Yang, J. Zeng, H. Lou, Z. Zeng, Q. Zeng. Phys. Rev. B **105**, *14*, 14420 (2022). https://doi.org/10.1103/PhysRevB.105.144201

[41] Y.M. Chen, T. Ohkubo, T. Mukai, K. Hono. J. Mater. Res. **24**, 1 (2009). https://doi.org/10.1557/jmr.2009.0001

[42] F. Meng, K. Tsuchiya, S. Li, Y. Yokoyama. Appl. Phys. Lett. **101**, *12*, 121914 (2012). http://dx.doi.org/10.1063/1.4753998

[43] G.E. Abrosimova, N.A. Volkov, A.S. Aronin. J. Surf. Investigation: X-ray, Synchrotron. Neutron Techniques **18**, *5*, 1155 (2024). https://doi.org/10.1134/S1027451024700964

[44] E.V. Boltynjuk, D.V. Gunderov, E.V. Ubyivovk, M.A. Monclús, L.W. Yang, J.M. Molina-Aldareguia, A.I. Tyurin, A.R. Kilmametov, A.A. Churakova, A.Yu. Churyumov, R.Z. Valiev. J. Alloys. Compd. **747**, 595 (2018). http://dx.doi.org/10.1016/j.jallcom.2018.03.018

[45] D. Gunderov, V. Astanin, A. Churakova, V. Sitdikov, E. Ubyivovk, A. Islamov, J.T. Wang. Metals **10**, *11*, 1433 (2020). https://doi.org/10.3390/met10111433

[46] R. Xiang, S. Zhou, B. Dong, G. Zhang, Z. Li, Y. Wang, C. Chang. Progr. Natural Sci. Mater. Intern. **24**, *6*, 649 (2014).

[47] C.F. Conde, J.S. Blazquez, A. Conde. In: Properties and Application of Nanocrystalline Alloys from Amorphous Precursor / Ed. B. Idzikowski. Kluwer Academic Publ., The Netherlands (2005). P. 111.

[48] N. Volkov, G. Abrosimova, A. Aronin. Mater. Lett. **265**, 127431 (2020). https://doi.org/10.1016/j.matlet.2020.127431

[49] G.E. Abrosimova, A.S. Aronin, N.A. Volkov. Phys. Solid State **61**, 1294 (2019). https://doi.org/10.1134/S1063783419070023

Translated by T.Zorina